

Completed Feature Disentanglement Learning for Multimodal MRIs Analysis

Tianling Liu, Hongying Liu, Fanhua Shang, Lequan Yu, Tong Han, Liang Wan

Abstract—Multimodal MRIs play a crucial role in clinical diagnosis and treatment. Feature disentanglement (FD)-based methods, aiming at learning superior feature representations for multimodal data analysis, have achieved significant success in multimodal learning (MML). Typically, existing FD-based methods separate multimodal data into modality-shared and modality-specific features, and employ concatenation or attention mechanisms to integrate these features. However, our preliminary experiments indicate that these methods could lead to a loss of shared information among subsets of modalities when the inputs contain more than two modalities, and such information is critical for prediction accuracy. Furthermore, these methods do not adequately interpret the relationships between the decoupled features at the fusion stage. To address these limitations, we propose a novel Complete Feature Disentanglement (CFD) strategy that recovers the lost information during feature decoupling. Specifically, the CFD strategy not only identifies modality-shared and modality-specific features, but also decouples shared features among subsets of multimodal inputs, termed as modality-partial-shared features. We further introduce a new Dynamic Mixture-of-Experts Fusion (DMF) module that dynamically integrates these decoupled features, by explicitly learning the local-global relationships among the features. The effectiveness of our approach is validated through classification tasks on three multimodal MRI datasets. Extensive experimental results demonstrate that our approach outperforms other state-of-the-art MML methods with obvious margins, showcasing its superior performance.

Index Terms—Multimodal learning, Feature disentanglement, Dynamic fusion, MRIs.

I. INTRODUCTION

Multi-modality data contains multiple aspects of information about an object, and different modalities can provide complementary information. Numerous previous studies have demonstrated the remarkable success of multimodal learning (MML) [1] for medical image analysis. However, inappropriate processing of multimodal information can significantly impact the efficiency of MML. According to [2], the key to successful MML lies in achieving a higher quality of feature representation. Many previous works [3]–[11] have focused on

T. Liu, F. Shang, L. Wan are with the College of Intelligence and Computing, Tianjin University, Tianjin, China.

H. Liu is with the Medical School of Tianjin University, Tianjin, China.

L. Yu is with the Department of Statistics and Actuarial Science, The University of Hong Kong, Hong Kong SAR, China.

T. Han is with the Brain Medical Center of Tianjin University, Huanhu Hospital, Tianjin, China.

Corresponding author: L. Yu (e-mail: lqyu@hku.hk) and L. Wan (e-mail: lwan@tju.edu.cn).

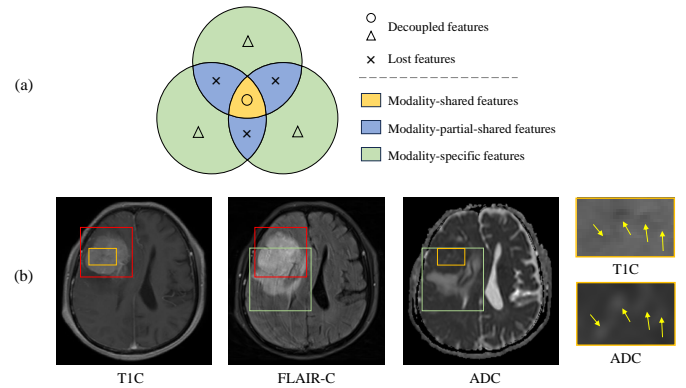


Fig. 1. Illustrations of incompletely represented features for existing feature disentanglement methods in the three-modal case. Sub-figure (a) presents a concept map, (b) shows a case in the Meningiomas dataset. In sub-figure (b), the tumor and edema areas are enclosed within the red and the green boxes respectively, and the yellow box indicates high cell density in tumor area. Notably, the location information of tumor and edema is shared across all three MRI series. Additionally, the tumor characteristic information is shared between the T1C and FLAIR-C series, the edema characteristics are shared between the FLAIR-C and ADC series, while the information regarding the cell density in tumor area is shared between the T1C and ADC series.

enhancing the learning performance, which can be classified into three categories. Two categories focus on extracting the shared information between multiple modalities [3], [4] or specific information of each modality [5], [6]. These methods cannot fully extract multimodal information, as they only focus on one type of feature, leading to information loss [10], [11]. The third category focuses on feature disentanglement (FD), which simultaneously decouples modality-shared features as well as modality-specific features [7]–[10], leading to sound results. These FD-based methods commonly enforce the following constraints on decoupled features: 1) modality-shared features should have higher similarity; 2) modality-specific features should have greater dissimilarity; and 3) modality-shared features and each modality-specific features should be as distinct as possible.

We revisit the relationship between the representation spaces of multimodal data. As illustrated in the concept map of the three-modal case in Fig. 1, intuitively, we can consider that there exists modality-shared information (yellow area) as well as modality-specific information (green area). Upon further consideration and exploration, we discover that there is shared information present between subsets of modalities (blue area). However, existing FD methods could potentially ignore such information due to the above three constraints, which only

account for modality-shared information and modality-specific information. On the other hand, our preliminary experiments reveals that the lost information is crucial for accurate prediction (see the first and fourth rows of Table IV). In Fig. 1 (b), we take meningiomas grading and invasion prediction data as an example for illustration. We can see that different MRI series provide specific information based on their distinct signal characteristics. The tumor area is highlighted in both T1C and FLAIR-C, indicating that these two modalities share information about the tumor. The edema area is highlighted in both FLAIR-C and ADC, indicating that both MRI series offer information about the edema characteristics. Additionally, T1C and ADC share information about the cell density in tumor area. In fact, such shared information among pairwise modalities is found to be relevant to the prediction of meningiomas grade and invasion in clinical research [12]–[14].

Furthermore, existing FD-based approaches also struggle with determining the optimal fusion methods for decoupled features. Current fusion studies mainly focus on uncertainty-based fusion methods [15], [16] and attention-based methods [17], [18]. Uncertainty-based methods may introduce more uncertainty when dealing with difficult-to-predict classes, potentially resulting in incorrect predictions. Attention-based methods perform feature fusion implicitly and cannot explicitly reveal the relationship between multiple features.

To tackle the above issues, we propose a completed feature disentanglement multimodal learning (CFDL) approach for multimodal MRIs analysis. First, we present a novel completed feature disentanglement (CFD) strategy to address the information loss in previous FD-based methods. In addition to decoupling modality-shared features among all modalities and modality-specific features, we further decouple features shared between subsets of modalities, referred to as *modality-partial-shared features*. The modality partial-shared features are also expected to have higher similarities, while to be dissimilar from the other two kinds of features. To improve the interpretability of feature fusion, we propose a new dynamic mixture-of-experts fusion (DMF) module, which can explicitly capture local-global interrelationships between the decoupled features for better fusion. In summary, our main contributions are summarized as follows:

- We find that existing FD-based MML methods suffer from the information loss due to incomplete feature decoupling and the lack of interpretability for the decoupled features fusion.
- We propose a novel CFD strategy to further decouple modality-partial-shared features to ensure completed feature decoupling from multimodal data. We demonstrate that these features play a crucial role in prediction.
- We introduce a new DMF module which can dynamically integrate the decoupled features while explicitly revealing the relationships between these features. This module enhances the interpretability of the fusion process.
- Experiments on three multimodal MRI datasets demonstrate the effectiveness and superiority of our framework compared to the state-of-the-art methods.

II. RELATED WORK

A. Feature Representation Learning in MML

Feature representation learning is a crucial aspect in the field of MML, which contains three types of methods. Some approaches [3], [4] have focused on the first type of method, which extracted specific features from each modality and subsequently fused them with obtained embeddings. Braman *et al.* [4] designed the Multimodal Orthogonalization (MMO) loss function to obtain the maximum specific representation for each of radiology, pathology, genomic and clinical data. Several methods [5], [6] have concentrated on the second type of method, which captured modality-shared features from multiple modalities. Ning *et al.* [6] built a bi-directional mapping between original space and shared space of multimodal to effectively obtained multi-modal shared representation. However, the first two type of methods have primarily emphasized either modality-specific or modality-shared features, thus failing to learn a comprehensive representation of multimodal data. The third type of method, FD, has proven to be effective in separating multimodal information into meaningful components and has been successfully applied in various applications [7]–[10]. Hu *et al.* [7] proposed a disentangled-multimodal adversarial autoencoder (DMM-AAE) model that employed a VAE to disentangle multimodal MRIs information into modal-common features and modal-specific features. However, this method only addressed the two-modal fusion scenario. Cheng *et al.* [9] extended this approach to multimodal fusion scenario. It is worth noting that both of these methods cannot be trained end-to-end due to the reliance on hand-crafted features as model inputs. Hazarika *et al.* [8] decoupled multimodal information into modality-invariant and modality-specific features using Central Moment Discrepancy metric, orthogonality constraints and reconstruction loss. Li *et al.* [10] proposed decoupled multimodal distillation (DMD), which first separated the representation of each modality into modality-irrelevant space and modality-exclusive space. Then, a graph distillation unit was employed to each space for dynamic enhancing the features of each modality.

The aforementioned FD methods have a common drawback that can result in incomplete feature representation learning in the case of three or more modalities, as depicted in Fig. 1. In contrast, the proposed CFD strategy addresses this limitation by decoupling multimodal information into modality-shared features, modality-specific features, and modality-partial-shared features, thereby enabling comprehensive feature representation learning.

B. Multimodal Feature Fusion

The fusion strategy is another crucial aspect of MML. Several approaches have involved concatenating features extracted from different modalities [3], [19] or representation spaces [7], [9], [10], such as modality-shared and modality-specific features. However, concatenation fusion has not effectively utilized the correlations between multiple modalities.

In recent years, there has been an increasing focus on exploring the correlations among multiple modalities to obtain effective features. Some methods achieve multimodal fusion

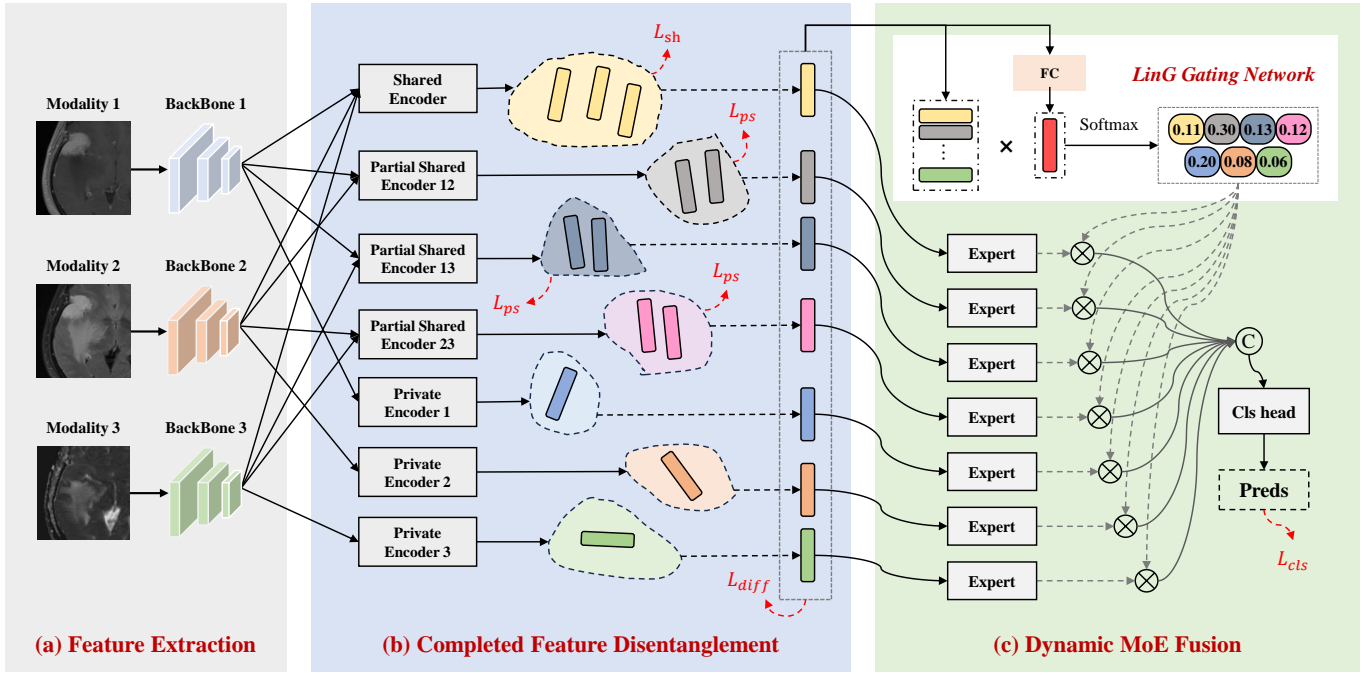


Fig. 2. The overview of proposed CFDL framework in the three-modal case. (a) For each modality, we adopt the same type of backbone for feature extraction. (b) Completed Feature Disentanglement (CFD) strategy decouples each extracted features to modality-shared features, modality-specific features, and modality-partial-shared features between pair-wise modalities. (c) Dynamic MoE Fusion (DMF) module dynamically and appropriately fuses decoupled features based on samples benefitted from LinG.GN. LinG.GN can obtain the complex interrelationships between these features. Specifically, © means concatenation operation, FC represents a fully-connected layer, $CLS\ head$ denotes a classification head.

by assigning weights or probabilities to each modality. Han *et al.* [15], [16] explored the uncertainties of different modalities to obtain reliable multimodal fusion information. Choi *et al.* [20] proposed EmbraceNet which performed multimodal representation fusion based on a probabilistic approach. However, these methods could be subject to the effect of difficult-to-predict classes. Zhou *et al.* [21] introduced a canonical correlation analysis (CCA)-based method named ADCCA to exploit the correlation between multiple modalities and integrate the complementary information from these modalities.

With the proven ability of attention mechanisms to enhance feature representation and explore complex correlation between multiple modalities, many attention-based multimodal fusion methods have emerged [17], [18], [22]–[24]. Zhang *et al.* [17] proposed a modality-aware mutual learning (MAML) framework that weighted the multimodal features using an attention-based modality-aware (MA) module. Zhu *et al.* [23] captured complementary information from multimodal data using self-attention and cross-modal attention, and further designed a triple network to obtain more discriminative information. Xing *et al.* [18] developed the NestedFormer framework, which included the Nested Modality-aware Feature Aggregation (NMaFA) module to explore long-range correlations within and between modalities for effective and comprehensive information learning. However, these attention-based methods cannot explicitly reveal the contribution of each decoupled features during fusion process.

Mixture-of-Experts (MoE) [25] employs multiple experts to extract distinct representation spaces from the input and generated corresponding weights using a gating network. MoE

have the ability to dynamically capture the mixture information from multiple experts. Several studies [26], [27] have extended MoE to handle multi-input scenarios, where each expert processes a specific input. These approaches leverage the dynamic nature of MoE. However, these methods concatenate all inputs to generate weights in the gating network without thoroughly considering the relationships between different inputs, which can limit the effectiveness of the fusion process. In contrast, we introduce a gating network to capture the local-global relationships between the decoupled features.

III. METHOD

Let's denote the input multimodal data as $\{X^i, y^i\}_{i=1}^N$, where N is the number of samples; $X^i = \{x_j^i\}_{j=1}^M$, M denotes the modality number of each sample; y^i is the classification label for the i -th sample.

A. Overview

The proposed CFDL framework, as shown in Fig. 2, consists of three parts: a) feature extraction from multimodal MRIs, b) completed feature disentanglement for feature decoupling, and c) dynamic MoE fusion for dynamically integrating the decoupled features. The framework employs the same type of backbone to extract latent features x_j from each modality. To capture a comprehensive representation of the multimodal data, the latent features are decoupled into modality-shared features, modality-specific features, and modality-partial-shared features using the proposed CFD strategy. The decoupled features are then integrated using the DMF

module. In the DMF module, each decoupled feature is paired with a specific expert, and a gating network named LinG_GN generates weights for multiple experts. The fused features are obtained by aggregating the weighted features from the experts. In the following, we take three-modal condition as examples to illustrate the proposed CFD strategy and DMF module.

B. Completed Feature Disentanglement Strategy

Inspired by previous FD methods [7]–[9], we first decouple the extracted latent features into modality-shared features and modality-specific features. We employ a shared-encoder \mathbf{E}_{sh} to decouple modality-shared features and three private-encoders \mathbf{E}_{sp}^j to decouple modality-specific feature for each modality. Three modality-shared features can be formulated as follows:

$$F_j = \mathbf{E}_{sh}(x_j), \quad (1)$$

and three modality-specific features can be obtained with:

$$P_j = \mathbf{E}_{sp}^j(x_j). \quad (2)$$

The *final modality-shared feature* F is the mean of all modality-shared features, given by

$$F = \frac{1}{M} \sum_j F_j. \quad (3)$$

We further consider modality-partial-shared features between pair-wise modalities. As a result, three groups of modality-partial-shared features are decoupled, with each group consisting of two features. The two features in the same group (G_{jk}^j, G_{jk}^k) are decoupled with the same partial-shared-encoder named \mathbf{E}_{ps}^{jk} , i.e.,

$$G_{jk}^j = \mathbf{E}_{ps}^{jk}(x_j), \quad G_{jk}^k = \mathbf{E}_{ps}^{jk}(x_k). \quad (4)$$

Specifically, G_{jk}^j represents the modality-partial-shared feature between the j -th modality and the k -th modality, which is decoupled from the j -th modality. The *final modality-partial-shared feature* G_{jk} can be calculated by averaging the modality-partial-shared features in each group,

$$G_{jk} = \frac{1}{2}(G_{jk}^j + G_{jk}^k). \quad (5)$$

In the end, we obtain three modality-shared features (F_1, F_2, F_3), three modality-specific features (P_1, P_2, P_3), and three groups of modality-partial-shared features including $\{G_{12}^1, G_{12}^2\}, \{G_{13}^1, G_{13}^3\}, \{G_{23}^2, G_{23}^3\}$. Furthermore, we get 7 *final decoupled features*, which is denoted as a set \mathcal{S} , where $\mathcal{S} = \{F, P_1, P_2, P_3, G_{12}, G_{13}, G_{23}\}$.

To enhance the completeness of the decoupled representation, we use the following three constraints:

- 1) Modality-shared features should exhibit high similarity to one another.
- 2) Modality-partial-shared features within each group should have maximum similarity.
- 3) The *final decoupled features* should exhibit maximum dissimilarity from one another.

To ensure the effective decoupling of modality-shared features and modality-partial-shared features, we employ the

mean squared error (MSE) loss as a constraint. The MSE loss measures the discrepancy between two features, and we aim to increase similarity between two features by minimizing this loss. The losses for modality-shared features \mathcal{L}_{sh} and modality-partial-shared features \mathcal{L}_{ps} are expressed as:

$$\mathcal{L}_{sh} = \sum_{j=1} \sum_{k=j+1} MSE(F_j, F_k), \quad (6)$$

$$\mathcal{L}_{ps} = \sum_{j=1} \sum_{k=j+1} MSE(G_{jk}^j, G_{jk}^k). \quad (7)$$

To enhance the decoupling of modality-specific features and minimize redundancy among all *final decoupled features*, we incorporate cosine similarity as a constraint for better optimization. Our objective is to increase the dissimilarity between the final decoupled features by reducing the cosine similarity between each pair of these features. The loss for all final decoupled features \mathcal{L}_{diff} is calculated by:

$$\mathcal{L}_{diff} = \sum_{j=1} \sum_{k=j+1} CS(\mathcal{S}_j, \mathcal{S}_k), \quad (8)$$

where $CS(\cdot, \cdot)$ represents the cosine similarity function.

C. Dynamic MoE Fusion Module

To ensure dynamic fusion of the final decoupled features, we introduce the DMF module based on the MoE architecture, which is shown in Fig. 2 (c). In DMF module, each final decoupled feature $\mathcal{S}_j \in \mathbb{R}^{dim}$ is associated with a specific expert $\mathbf{E}x_j$, which is implemented as a fully-connected layer. We introduce LinG_GN to dynamically generate weights for these experts, taking into account the relationships of these final decoupled features. The LinG_GN operates with two inputs to capture a comprehensive understanding of these features. Firstly, we concatenate all the final decoupled features as one input for the LinG_GN. To integrate this concatenated feature, we map the concatenated feature into a unified representation utilizing a fully-connected layer FC . This unified representation captures the collective information from all the final decoupled features and is treated as the global feature $g \in \mathbb{R}^{dim}$,

$$g = FC(ReLU(Cat(\mathcal{S}_1, \dots, \mathcal{S}_7))), \quad (9)$$

where $Cat(\cdot, \dots, \cdot)$ means column concatenation operation and $ReLU$ is the activation function. Secondly, we stack all the final decoupled features as the second input for the LinG_GN. This stacked features retain the individual information from each final decoupled feature and are considered as the local features, denoted as $\mathbf{O} = [\mathcal{S}_1^T, \dots, \mathcal{S}_7^T]$, where $\mathbf{O} \in \mathbb{R}^{7 \times dim}$. By obtaining both the global feature and the local features, we can explore the importance of each local feature within the context of the global feature. This exploration allows us to determine the weight ω of local features in contributing to the fused representation. The weight ω is calculated by:

$$\omega = softmax(\mathbf{O} \times g), \quad (10)$$

where \times represents matrix multiplication operation, $\omega \in \mathbb{R}^7$. Each element in ω represents the weight for the corresponding

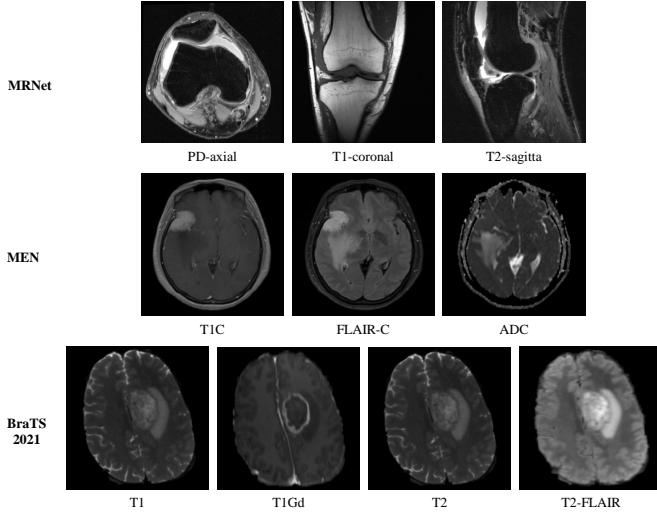


Fig. 3. The display of cases from three multimodal MRI datasets.

expert network $E\mathbf{x}_j$. The fused feature F_f is obtained by concatenating the linearly weighted experts,

$$F_f = \text{Cat}(\omega_1 E\mathbf{x}_1(\mathcal{S}_1), \dots, \omega_7 E\mathbf{x}_7(\mathcal{S}_7)). \quad (11)$$

For the final prediction \hat{y} , we utilize a Multi-Layer Perceptron (*MLP*) as the classifier. The cross-entropy (CE) loss is employed as the supervision for prediction. The classification loss \mathcal{L}_{cls} is defined as:

$$\mathcal{L}_{cls} = CE(\hat{y}, y). \quad (12)$$

The final loss \mathcal{L} can be defined as the weighted sum of aforementioned losses,

$$\mathcal{L} = \mathcal{L}_{cls} + \alpha(\mathcal{L}_{sh} + \mathcal{L}_{ps}) + \beta\mathcal{L}_{diff}, \quad (13)$$

where α and β are balance factors.

D. Network Architecture

We utilize the 3D ResNet18 [28] as the backbone for feature extraction, and the parameters of these backbones are not shared. The dimension of the each extracted latent feature x_j is 512. The shared-encoder E_{sh} , each private-encoders E_{sp}^j , each partial-shared-encoders E_{ps}^{jk} , FC and each expert $E\mathbf{x}_j$ are all implemented as one fully-connected layer with dim neurons. The *MLP* consists of two fully-connected layers with dim neurons and one output layer with num_cls neurons, where num_cls represents the number of classes. Each fully-connected layer in *MLP* is followed by a ReLU layer and a Dropout layer. We empirically set dim as 32.

IV. EXPERIMENTS

A. Datasets and Tasks

We utilize three multimodal MRI datasets, which consist of two public datasets and one private dataset, to verify the effectiveness of the proposed framework. Some cases from these three datasets are shown in Fig 3.

1) *Meniscal Tear Prediction*: For the prediction of meniscal tear, we employ the MRNet dataset [29], which is a publicly available knee multi-MRI dataset¹. There are 1130 cases in training set and 120 cases in validation set. The training set contains 397 meniscal tear cases and 733 contrast cases, and the validation set contains 52 meniscal tear cases and 68 contrast cases. Each case includes three MRIs: sagittal plane T2-weighted series (T2-sagittal), coronal plane T1-weighted series (T1-coronal) and axial plane PD-weighted series (PD-axial). We resize the MRIs to $24*128*128$ as the inputs of the framework.

2) *Meningiomas Grading Prediction*: We collect Meningiomas Grading Prediction Dataset, referred to as MEN, from the Brain Medical Center of Tianjin University, Tianjin Huanhu Hospital². This dataset consists of three grades of meningiomas: Grade 1 (G1), Grade 2 with invasion (G2inv) and Grade 2 without invasion (G2ninv). The total dataset comprises 798 cases, including 650 Grade_1, 62 Grade_2inv and 86 Grade_2ninv cases. Each case includes three brain MRIs: Contrast-Enhanced T1 series (T1C), Contrast-Enhanced T2 FLAIR series (FLAIR-C) and Apparent Diffusion Coefficient series (ADC). Following previous works [30], [31], we request radiologists to crop the regions of interest (ROIs). To maintain the shape of the tumor and edema regions, the ROIs are zero-padded into squares and resized to dimensions of $24*128*128$, which serve as the inputs for the framework.

3) *MGMT Promoter Status Prediction*: The MGMT Promoter Status Prediction Dataset, known as BraTS 2021 [32], is a publicly available multimodal brain MRI dataset. It encompasses cases with MGMT methylated (MGMT+) and unmethylated (MGMT-) status. The dataset comprises 580 available cases³, with each case containing four modalities: T1, post-contrast T1-weighted (T1Gd), T2-weighted (T2), and T2 Fluid Attenuated Inversion Recovery (T2-FLAIR). Specifically, there are 275 MGMT- cases and 305 MGMT+ cases. Pre-processing for each modality involves image registration and skull-stripping using the Cancer Imaging Phenomics Toolkit (CaPTk) [33]. We crop the ROIs using masks generated by the pretrained Swin UNETR [34]. Finally, we zero-pad the ROIs into squares and resize them to $16*128*128$ as the inputs for the proposed framework.

B. Implementation Details

1) *Training Details*: We employ 3-fold cross-validation for private MEN and public BraTS 2021 datasets, and train three times using different seeds with already divided training and validation data for MRNet dataset. During model training, we implement several techniques to prevent overfitting, such as data augmentation, L2 regularization (weight decay) and

¹More information about the MRNet dataset can be available in <https://stanfordmlgroup.github.io/competitions/mrnet/>.

²The Ethical Committee of Tianjin Huanhu Hospital approves scientific research using these MRIs and waives the need for informed patient consent ((Jinhuan) Ethical Review No.(2022-046)).

³We drop 5 cases from original 585 cases during pre-processing. There are 3 cases with unexpected issues. The other 2 cases cannot be registered by CaPTk. Get more information in <https://www.kaggle.com/c/rsna-miccai-brain-tumor-radiogenomic-classification>.

dropout [35]. Data augmentation techniques include random clip, random crop, gaussian noise and random erasing [36]. The weight decay is set as $1e-4$, and the dropout value is set to 0.5. The network is optimized with the Adam optimizer [37]. We linearly warm up the learning rate from zero to the preset value over 5 epochs and apply a learning rate decay strategy, reducing the learning rate to 0.8 after every 5 epochs. The batch size is set 32. For MRNet dataset, we initialize the learning rate value as $8e-4$, and set the number of epochs to 50. The balance factors, α and β , are set to 0.5 and 0.005 respectively. For MEN dataset, the learning rate is specified as $5e-4$, and number of epochs is fixed as 100. Both α and β are set as 1. For BraTS 2021 dataset, we preset the learning rate value as $2e-4$ and the number of epochs as 50. We fix both α and β as 0.001. All experiments are conducted with PyTorch on an NVIDIA RTX 3090 GPU.

2) Evaluation Metrics: For two-class datasets, MRNet and BraTS 2021, we employ seven metrics to assess the effectiveness of the proposed framework, including Sensitivity (SEN), Specificity (SPE), Accuracy (ACC), G-mean, Balanced Accuracy (Ba_ACC) [38], Area Under the Precision-Recall Curve (AUPRC), Area Under the Curve (AUC). For three-class dataset, MEN, we utilize seven evaluation metrics, including Accuracy (ACC), Accuracy of G1 (ACC_G1), Accuracy of G2inv (ACC_G2inv), Accuracy of G2ninv (ACC_G2ninv), weighted F1 score (weighted-F1), macro F1 score (macro-F1) and AUC. For the statistical analysis, Wilcoxon signed-rank [39] is adopted to compare the metrics of our proposed framework with other methods.

3) Compared Methods: We compare the proposed framework with seven state-of-the-art (SOTA) MML methods, including EmbraceNet [20], ETMC [16], ADCCA [21], MAML [17], NestedFormer [18], MISA [8], DMD [10]. Specifically, ETMC is a uncertainty-based MML method. ADCCA is a CCA-based MML method. MAML and NestedFormer are attention-based MML methods originally designed for segmentation, but adapted to the classification task by adding a classifier after the encoders. MISA and DMD are FD-based MML methods. To ensure a fair comparison, in addition to the transformer-based NestedFormer method, we set the backbones of other CNN-based comparison methods to be the same as that of the proposed framework.

C. Quantitative Results

1) Evaluation on Meniscal Tear Prediction Dataset: The comparison results on the MRNet dataset are summarized in Table I. Among the comparison methods, the FD-based method DMD [10] achieves the best AUC (0.7668), while the uncertainty-based method ETMC [16] obtains the second place (0.7655). The attention-based method MAML [17] obtains better results than other comparison methods in three metrics: ACC (0.7306), Ba_ACC (0.7261) and AUPRC (0.6148). Our proposed framework achieves the first place in five metrics: ACC (0.7389, 0.0083 better than the 2nd), G-Mean (0.7351, 0.0096 better than the 2nd), Ba_ACC (0.7372, 0.0111 better than the 2nd), AUPRC (0.6207, 0.0059 better than the 2nd) and AUC (0.8029, 0.0361 better than the 2nd). The higher

TABLE I
THE COMPARISON RESULTS ON THE MRNET DATASET (MEAN \pm STANDARD DEVIATION). THE BEST AND SECOND BEST RESULTS FOR EACH METRIC ARE RESPECTIVELY HIGHLIGHTED BY RED AND BLUE. THE MARKER "*" INDICATES THAT OUR PROPOSED FRAMEWORK ACHIEVES STATISTICALLY SIGNIFICANT RESULTS THAN OTHER METHODS (P-VALUE<0.05).

Method	SEN	SPE	ACC	G-Mean	Ba_ACC	AUPRC	AUC
EmbraceNet [20]	0.6410* ± 0.0111	0.7696 ± 0.0424	0.7139* ± 0.0192	0.7021* ± 0.0136	0.7053* ± 0.0157	0.5924* ± 0.0199	0.7509* ± 0.0136
MISA [8]	0.6795* ± 0.0111	0.7451 ± 0.0557	0.7167* ± 0.0289	0.7111* ± 0.0232	0.7123* ± 0.0249	0.5963* ± 0.0314	0.7517* ± 0.0294
MAML [17]	0.6923 ± 0.1071	0.7598 ± 0.1390	0.7306 ± 0.0337	0.7183* ± 0.0200	0.7261* ± 0.0186	0.6148 ± 0.0346	0.7609* ± 0.0068
ETMC [16]	0.7949 ± 0.0675	0.6274* ± 0.0946	0.7000* ± 0.0300	0.7031* ± 0.0268	0.7111* ± 0.0224	0.5834* ± 0.0266	0.7655* ± 0.0169
NestedFormer [18]	0.7308 ± 0.0193	0.7206* ± 0.0255	0.7250* ± 0.0167	0.7255* ± 0.0159	0.7257* ± 0.0160	0.6042* ± 0.0174	0.7540* ± 0.0113
ADCCA [21]	0.7500 ± 0.0693	0.6765* ± 0.0589	0.7083* ± 0.0084	0.7104* ± 0.0096	0.7133* ± 0.0094	0.5882* ± 0.0073	0.7627* ± 0.0050
DMD [10]	0.6154* ± 0.1201	0.7990 ± 0.0945	0.7195* ± 0.0048	0.6955* ± 0.0244	0.7072* ± 0.0136	0.5997* ± 0.0051	0.7668* ± 0.0112
Proposed	0.7244 ± 0.0588	0.7500 ± 0.0778	0.7389 ± 0.0255	0.7351 ± 0.0178	0.7372 ± 0.0199	0.6207 ± 0.0301	0.8029 ± 0.0219

TABLE II
THE COMPARISON RESULTS ON THE MEN DATASET (MEAN \pm STANDARD DEVIATION). THE BEST AND SECOND BEST RESULTS FOR EACH METRIC ARE RESPECTIVELY HIGHLIGHTED BY RED AND BLUE.

Method	ACC	ACC_G1	ACC_G2inv	ACC_G2ninv	weighted-F1	macro-F1	AUC
EmbraceNet [20]	0.9136* ± 0.0103	0.9570 ± 0.0206	0.7894* ± 0.0353	0.6730* ± 0.1192	0.9155* ± 0.0100	0.8053* ± 0.0329	0.8683* ± 0.0286
MISA [8]	0.9099* ± 0.0103	0.9678 ± 0.0199	0.8848 ± 0.0603	0.4873* ± 0.0535	0.9056* ± 0.0074	0.7885* ± 0.0301	0.9411* ± 0.0092
MAML [17]	0.9360* ± 0.0107	0.9707 ± 0.0209	0.9015 ± 0.0523	0.6992* ± 0.1059	0.9361* ± 0.0076	0.8524* ± 0.0076	0.9600* ± 0.0113
ETMC [16]	0.8834* ± 0.0088	0.9385* ± 0.0138	0.8045* ± 0.0569	0.5198* ± 0.1783	0.8836* ± 0.0158	0.7595* ± 0.0512	0.9051* ± 0.0364
NestedFormer [18]	0.9273* ± 0.0060	0.9584 ± 0.0167	0.8212* ± 0.0620	0.7682* ± 0.0468	0.9298* ± 0.0036	0.8436* ± 0.0030	0.9695* ± 0.0083
ADCCA [21]	0.8295* ± 0.0446	0.9091* ± 0.0698	0.5803* ± 0.1253	0.4119* ± 0.2221	0.8284* ± 0.0301	0.6289* ± 0.0534	0.8753* ± 0.0421
DMD [10]	0.8897* ± 0.0076	0.9677 ± 0.0002	0.8030* ± 0.1046	0.3619* ± 0.0644	0.8798* ± 0.0101	0.7303* ± 0.0279	0.9202* ± 0.0227
Proposed	0.9462 ± 0.0113	0.9616 ± 0.0160	0.9182 ± 0.0315	0.8492 ± 0.0383	0.9483 ± 0.0101	0.8936 ± 0.0106	0.9776 ± 0.0021

ACC and AUC, along with the more balanced accuracy between positive and negative cases, demonstrate the effectiveness of our proposed framework on the MRNet dataset.

2) Evaluation on Meningiomas Grading Prediction Dataset: We further validate the proposed framework on the private MEN dataset, and the comparison results are shown in Table II. Among the comparison methods, the attention-based method NestedFormer achieves the best AUC (0.9695) and ACC_G2ninv (0.7682). The other attention-based method, MAML, achieves better results than other comparison methods in five metrics, including ACC (0.9360), ACC_G1 (0.9707), ACC_G2inv (0.9015), weighted-F1 (0.9361) and macro-F1 (0.8524). The reason for the poor performance of DMD is that the difficult prediction of class G2ninv results in distillation leaning towards other classes. In contrast, our proposed framework achieves first place in six metrics: ACC (0.9462, 0.0102 better than the 2nd), ACC_G2inv (0.9182, 0.0167 better than the 2nd), ACC_G2ninv (0.8492, 0.0810 better than the 2nd), weighted-F1 (0.9483, 0.0122 better than the 2nd), macro-F1 (0.8936, 0.0412 better than the 2nd) and AUC (0.9776, 0.0081 better than the 2nd). Benefit from the CFD strategy and DMF module, our proposed framework achieves relatively high and

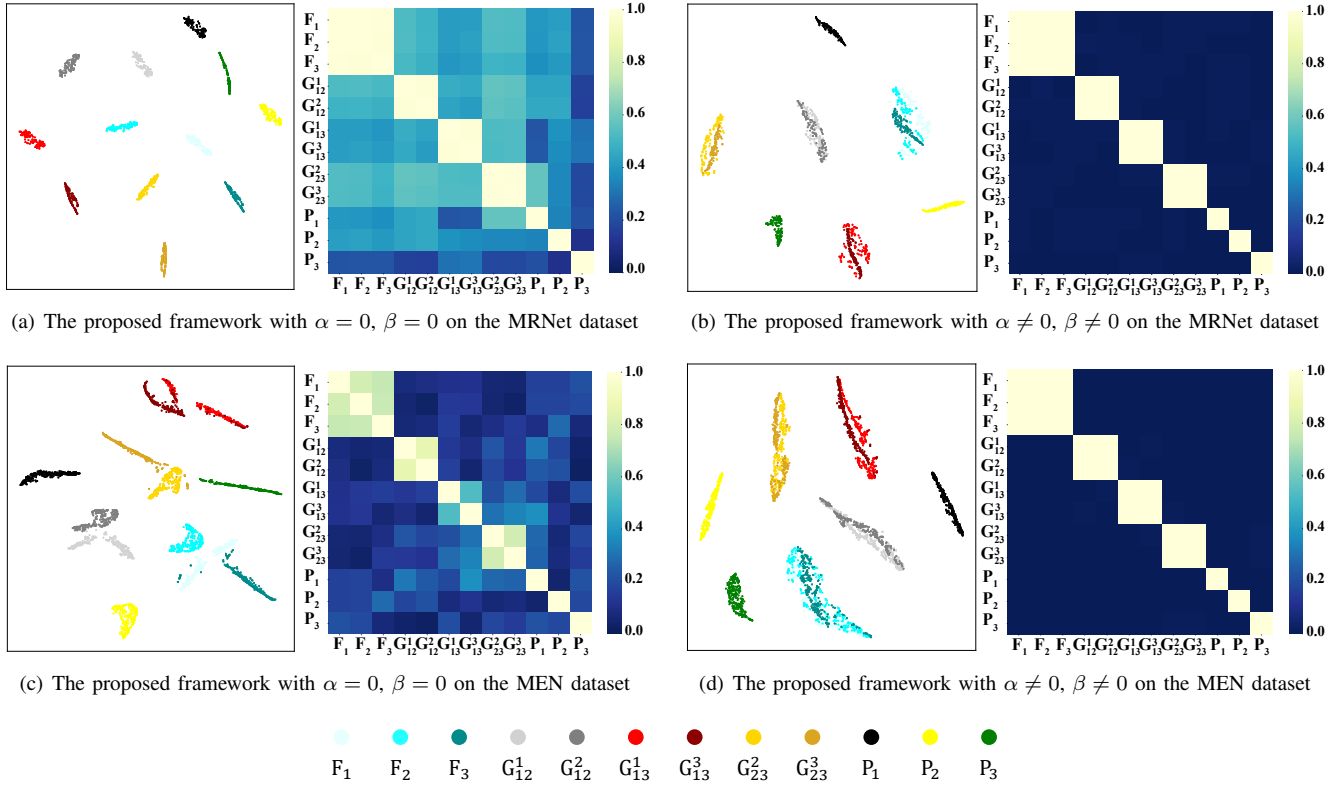


Fig. 4. Visualization results of the proposed framework on the MRNet and MEN datasets. In each sub-figure, the left part displays t-SNE visualization of the decoupled features, and the right part shows the heatmap which displays the cosine similarity of each pair-wise decoupled features. In the heatmap, the closer the color is to yellow, the greater the similarity between the two features. Conversely, the closer the color is to blue, the smaller the similarity between the two features.

balanced accuracy on each class.

In addition, the statistical test results on both datasets, as shown in Table I and Table II, further indicate that our proposed framework significantly outperforms the comparison methods in most metrics.

D. Ablation Analysis

We also verify the effectiveness of the proposed CFD strategy and DMF module. Ablation studies are conducted on both adopted datasets, and the results are summarized in Table III and Table IV, respectively. In the tables, the models are termed as baseline1, baseline2, ..., baseline6 from the top row to the bottom row, with baseline6 representing the proposed framework. The ablation studies consider three factors: *dis_ps*, *MoE* and *LinG*. The *dis_ps* factor, which related to CFD strategy, determines whether to decouple modality-partial-shared features during the feature decoupling process. There are two factors related to the DMF module, namely *MoE* and *LinG*. The *MoE* factor represents whether to adopt MoE for the feature fusion, with “ \times ” indicating fusion with concatenation operation. The *LinG* factor denotes whether to utilize proposed LinG.GN to generate weights in MoE, with “ \times ” representing the use of concatenation of decoupled features as the input of the gating network. The concatenation operation for inputs in gating network is the common setting in MoE-based MML methods [27], [40].

TABLE III
THE ABLATION STUDY OF THE PROPOSED FRAMEWORK ON THE MRNET DATASET.

Proposed			SEN	SPE	ACC	G-Mean	Ba_ACC	AUPRC	AUC
<i>dis_ps</i>	MoE	LinG							
\times	\times	-	0.6859	0.7157	0.7028	0.6988	0.7008	0.5817	0.7544
\times	\checkmark	\times	0.6859	0.7108	0.7000	0.6874	0.6983	0.5810	0.7566
\times	\checkmark	\checkmark	0.7885	0.6863	0.7306	0.7326	0.7374	0.6114	0.7672
\checkmark	\times	-	0.7436	0.7255	0.7333	0.7298	0.7346	0.6142	0.7745
\checkmark	\checkmark	\times	0.7820	0.6569	0.7111	0.7151	0.7195	0.5917	0.7591
\checkmark	\checkmark	\checkmark	0.7244	0.7500	0.7389	0.7351	0.7372	0.6207	0.8029

TABLE IV
THE ABLATION STUDY OF THE PROPOSED FRAMEWORK ON THE MEN DATASET.

Proposed			ACC	ACC_G1	ACC_G2inv	ACC_G2ninv	weighted -F1	macro -F1	AUC
<i>dis_ps</i>	MoE	LinG							
\times	\times	-	0.9076	0.9371	0.9333	0.6635	0.9113	0.8091	0.9584
\times	\checkmark	\times	0.9265	0.9539	0.8106	0.8072	0.9302	0.8549	0.9590
\times	\checkmark	\checkmark	0.9326	0.9525	0.8515	0.8397	0.9364	0.8634	0.9699
\checkmark	\times	-	0.9101	0.9232	0.8833	0.8278	0.9171	0.8355	0.9638
\checkmark	\checkmark	\times	0.9297	0.9491	0.8364	0.8270	0.9314	0.8563	0.9745
\checkmark	\checkmark	\checkmark	0.9462	0.9616	0.9182	0.8492	0.9483	0.8936	0.9776

Specifically, the order of the three modalities is PD-axial, T1-coronal and T2-sagittal on the MRNet dataset, and TIC, Flair-C, ADC on the MEN dataset.

1) *Effectiveness of the CFD Strategy*: In Table III, using *dis_ps* consistently results in significant improvements when using the same settings of factors *MoE* and *LinG* on the

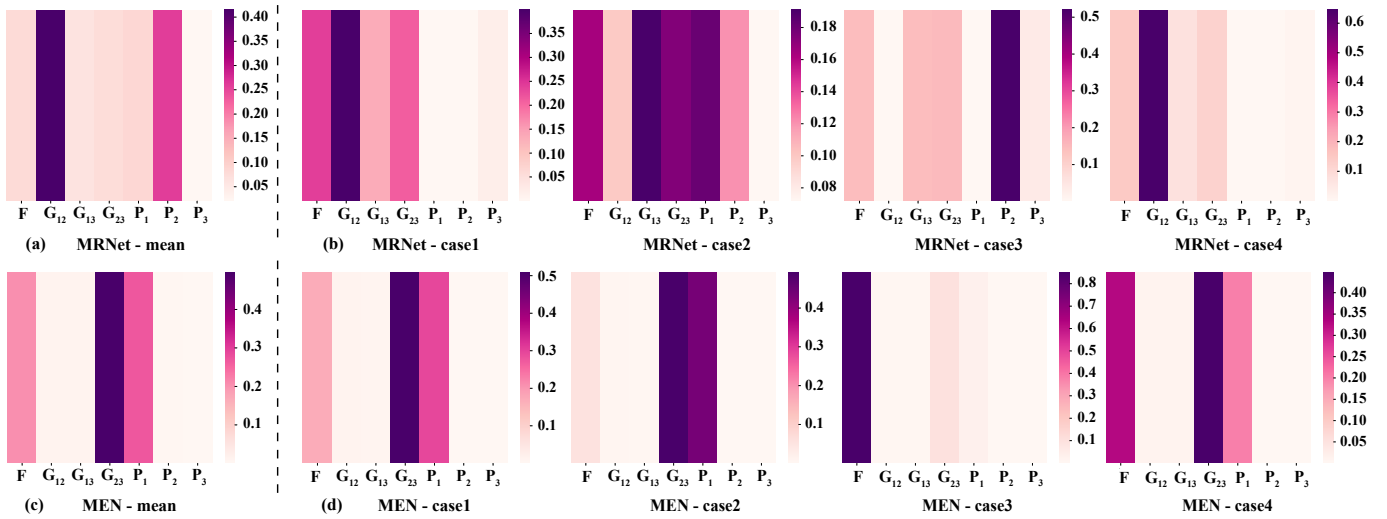


Fig. 5. Heatmaps of feature weights in DMF module on the MRNet and MEN datasets. (a) and (c) show the mean feature weights of all test data on both datasets. (b) and (d) display the feature weights of four cases in each dataset, respectively.

MRNet dataset (see baseline1 and baseline4, or baseline2 and baseline5, or baseline3 and baseline6). Similar results are obtained on the MEN dataset (see Table IV). These ablation studies on the *dis.ps* factor validate the effectiveness of the proposed CFD strategy.

We also visualize the distribution of the decoupled features using t-SNE [41], and draw the heatmap which displays the cosine similarity between each pair of these features. Fig. 4 (b) shows the visualization results for MRNet dataset. These visualization results meet the three principles which we described in Sec. III-B.

- 1) Modality-shared features including F_1 , F_2 and F_3 cluster together in the t-SNE visualization. These features have a cosine similarity value of 1 with each other as shown in the corresponding heatmap.
- 2) Modality-partial-shared features in each group exhibit a high degree of similarity. For example, when considering the two features (G_{12}^1 , G_{12}^2) from the same group, t-SNE visualization reveals overlaps between these representations. Additionally, the heatmap shows a cosine similarity value of 1 between them.
- 3) There are relatively far distance between the final modality-shared feature, each final modality-partial-shared feature and each modality-specific feature, as shown in the t-SNE visualization. These features have a vary small cosine similarity value with each other as shown in the heatmap.

Similar visualization results are observed on the MEN dataset, as depicted in Fig. 4 (d).

Furthermore, we conduct ablation studies for α and β on both adopted datasets, as shown in Fig. 4. Specifically, α and β are balance factors of losses related to the CFD strategy (\mathcal{L}_{sh} , \mathcal{L}_{ps} and \mathcal{L}_{diff}). For both datasets, the comparison results (see sub-figure (a) and (b) for MRNet dataset and sub-figure (c) and (d) for MEN dataset) clearly demonstrate that both modality-shared features and modal-partial-features are better learnt when using CFD-related losses ($\alpha \neq 0$, $\beta \neq 0$).

2) Effectiveness of the DMF Module: The ablation results on the MRNet dataset are shown in Table III. From this table, we observe that using the factor *MoE* and *LinG* can improve the performance when not using *dis.ps* (see baseline1, baseline2 and baseline3). But when using *dis.ps*, the performance of using *MoE* is lower than that of without *MoE* (see baseline4 and baseline5). The possible reason is that simple concatenation used in the gating network cannot effectively capture the relationship between the final decoupled features as the number of these features increased. In contrast, our proposed LinG_GN can dynamically capture the complex relationship between these features, allowing for better weighting and ultimately achieving improved prediction performance (see baseline4, baseline5 and baseline6). The ablation studies on the MEN dataset are shown in Table IV. Our proposed DMF module achieves the best performance on both MRNet and MEN datasets.

Moreover, we draw heatmaps of weights for the final decoupled features learned in the LinG_GN. Fig. 5 (a) and (b) show the heatmaps on the MRNet dataset. Firstly, we plot the mean weight of all cases in the test set for each final decoupled feature in a heatmap named *MRNet-mean* (see Fig. 5 (a)). This heatmap illustrates that G_{12} and P_2 play greater roles during feature integration, with G_{12} obtaining a maximum weight of around 0.4. Specifically, G_{12} represents the final modality-partial-shared feature between PD-axial and T1-corona, and P_2 represents modality-specific feature of T1-corona. Additionally, we randomly display the heatmaps of four cases (see Fig. 5 (b)).

The heatmaps on the MEN dataset are shown in Fig. 5 (c) and (d), indicating that F , G_{23} and P_1 have more important roles during feature fusion, with G_{23} obtaining the maximum weights, almost reaching 0.5. Specifically, F represents the final modality-shared feature, G_{23} represents the final modality-partial-shared feature between FLAIR-C and ADC, and P_1 represents the modality-specific feature of T1C.

These heatmaps on both adopted datasets demonstrate that our proposed DMF module can dynamically capture the re-

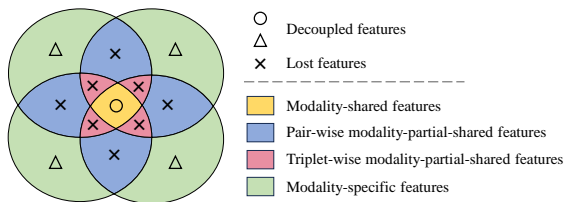


Fig. 6. Illustration of incomplete feature representation on the existing FD methods in four-modal condition. Both modality-partial-shared features between pair-wise modalities (blue area) and triplet-wise modalities (red area) are lost.

relationships between the decoupled features across different samples (see Fig. 5 (b) for the MRNet dataset and Fig. 5 (d) for the MEN dataset). Moreover, there are modality-partial-shared features playing important roles during feature fusion on both datasets, further illustrating the necessity of the CFD strategy.

V. DISCUSSION

A. Evaluation in the Four-modal Case

In order to assess the generalization of the proposed framework on a wider range of modalities, we extend the proposed framework to MGMT promoter status prediction dataset (BraTS 2021) in the four-modal case, and the concept map is shown in Fig. 6. In this case, the complexity increases as we needed to decouple not only the pair-wise modality-partial-shared features but also the triplet-wise modality-partial-shared features. This leads to a total of 32 decoupled features and 15 final decoupled features.

The comparison results on BraTS 2021 dataset are listed in Table V. The seven SOTA methods obtain comparable results. Our proposed framework achieves the best results in five metrics, including ACC (0.6137, 0.0121 better than the 2nd), G-Mean (0.6089, 0.0114 better than the 2nd), Ba_ACC (0.6123, 0.0127 better than the 2nd), AUPRC (0.5934, 0.0085 better than the 2nd), AUC (0.6177, 0.0173 better than the 2nd). The statistical test results obtained on the BraTS 2021 dataset are similar to those of the MRNet and MEN datasets.

However, it is important to acknowledge that as the number of modalities increases, the relationships between multiple modalities become more intricate, posing challenges for the CFD strategy. The inclusion of more modalities as inputs leads to an increase in network parameters, thereby exacerbating the difficulty of network optimization. However, in clinical studies, commonly used multimodal MRI datasets typically contain two to four modalities. Our proposed framework has been designed to achieve effective performance under these conditions.

B. Computational Complexity Analysis

As shown in Table VI, we compare the number of parameters and GFLOPS between the proposed method and the comparison methods. Specifically, we only consider the comparison methods that adopt the same backbone as the proposed method. In the three-modal case, the proposed method achieves best performance with the fewest parameters and

TABLE V
THE COMPARISON RESULTS ON THE BRATS 2021 DATASET (MEAN±STANDARD DEVIATION). THE BEST AND SECOND BEST RESULTS FOR EACH METRIC ARE HIGHLIGHTED BY RED AND BLUE.

Method	SEN	SPE	ACC	G-Mean	Ba_ACC	AUPRC	AUC
EmbraceNet [20]	0.6034 ± 0.1006	0.5200 ± 0.1484	0.5639* ± 0.0213	0.5506* ± 0.0358	0.5617* ± 0.0269	0.5610* ± 0.0180	0.5942* ± 0.0412
MISA [8]	0.5515* ± 0.0991	0.6428 ± 0.0966	0.5948* ± 0.0288	0.5905* ± 0.0294	0.5972* ± 0.0281	0.5849* ± 0.0190	0.5992* ± 0.0373
MAML [17]	0.7353 ± 0.1172	0.4427* ± 0.1313	0.5966* ± 0.0250	0.5607* ± 0.0503	0.5890* ± 0.0260	0.5765* ± 0.0164	0.6004* ± 0.0060
ETMC [16]	0.7275 ± 0.1158	0.4620* ± 0.0974	0.6016* ± 0.0171	0.5732* ± 0.0154	0.5948* ± 0.0129	0.5798* ± 0.0071	0.5958* ± 0.0332
NestedFormer [18]	0.5934* ± 0.1240	0.6037 ± 0.0879	0.5982* ± 0.0237	0.5921* ± 0.0214	0.5985* ± 0.0182	0.5842* ± 0.0104	0.5962* ± 0.0236
ADCCA [21]	0.6390 ± 0.0446	0.5602 ± 0.0383	0.6016* ± 0.0171	0.5975* ± 0.0158	0.5996* ± 0.0167	0.5843* ± 0.0107	0.6003* ± 0.0303
DMD [10]	0.6654 ± 0.0229	0.5059* ± 0.0604	0.5898* ± 0.0223	0.5792* ± 0.0293	0.5857* ± 0.0239	0.5750* ± 0.0160	0.5686* ± 0.0159
Proposed	0.6397 ± 0.0605	0.5849 ± 0.0806	0.6137 ± 0.0075	0.6089 ± 0.0136	0.6123 ± 0.0108	0.5934 ± 0.0089	0.6177 ± 0.0205

TABLE VI

THE COMPUTATIONAL COMPLEXITY COMPARISON BETWEEN PROPOSED AND COMPARISON METHODS IN THE THREE-MODAL CASE AND FOUR-MODAL CASE.

Methods	Three-modal		Four-modal	
	Parameters (M)	GFLOPS	Parameters (M)	GFLOPS
EmbraceNet [20]	99.62	46.16	132.78	32.23
MISA [8]	100.72	46.17	134.22	45.44
MAML [17]	103.26	165.63	137.63	111.93
ETMC [16]	101.62	46.17	135.44	45.44
ADCCA [21]	99.93	46.16	133.24	45.44
DMD [10]	104.22	46.27	142.75	45.67
Proposed	99.62	46.16	132.89	45.44

the lowest GFLOPS. In the four-modal case, the EmbraceNet method has the fewest parameters and GFLOPS, but our proposed method achieves a significant performance improvement using a similar number of parameters and the second-fewest GFLOPS. The number of parameters of all methods increases from the three-modal case to the four-modal case. However, our proposed method achieves a better performance improvement with a relatively small increase in parameters.

VI. CONCLUSION AND FUTURE WORK

In this paper, we propose an effective MML framework named CFDL. More importantly, we present a novel CFD strategy that separates multimodal information into modality-shared features, modality-specific features and modality-partial-shared features, where the latter are overlooked in previous FD-based methods. Our analysis and experiments demonstrate the significant roles played by modality-partial-shared features in prediction. Additionally, we present the DMF module, which dynamically fuses decoupled features in an explicit manner. The proposed LinG-GN in the DMF module can generate weights for the decoupled features by learning local-global relationship between these features. This customized fusion module can provide interpretability for clinical analysis, enabling a deeper understanding of the characteristics and behaviors of each decoupled features. Experimental results on three multimodal MRI datasets verify the effectiveness of the proposed framework. Moreover, the visualization results provide evidence for the benefits of our CFD strategy in achieving comprehensive and informative feature decoupling,

and the DMF module in enabling dynamic fusion of the decoupled features. Furthermore, we consider that the underlying principles of proposed framework can be extended to other medical imaging tasks. In the future, we plan to explore the application of our framework to medical segmentation tasks, which are closely related to medical classification tasks.

REFERENCES

- [1] T. Baltrušaitis, C. Ahuja, and L.-P. Morency, "Multimodal machine learning: A survey and taxonomy," *IEEE transactions on pattern analysis and machine intelligence*, vol. 41, no. 2, pp. 423–443, 2018.
- [2] Y. Huang, C. Du, Z. Xue, X. Chen, H. Zhao, and L. Huang, "What makes multi-modal learning better than single (provably)," *Advances in Neural Information Processing Systems*, vol. 34, pp. 10944–10956, 2021.
- [3] X. He, Y. Deng, L. Fang, and Q. Peng, "Multi-modal retinal image classification with modality-specific attention network," *IEEE transactions on medical imaging*, vol. 40, no. 6, pp. 1591–1602, 2021.
- [4] N. Braman, J. W. Gordon, E. T. Goossens, C. Willis, M. C. Stumpe, and J. Venkataraman, "Deep orthogonal fusion: multimodal prognostic biomarker discovery integrating radiology, pathology, genomic, and clinical data," in *Medical Image Computing and Computer Assisted Intervention–MICCAI 2021: 24th International Conference, Strasbourg, France, September 27–October 1, 2021, Proceedings, Part V 24*. Springer, 2021, pp. 667–677.
- [5] T. Zhou, M. Liu, H. Fu, J. Wang, J. Shen, L. Shao, and D. Shen, "Deep multi-modal latent representation learning for automated dementia diagnosis," in *Medical Image Computing and Computer Assisted Intervention–MICCAI 2019: 22nd International Conference, Shenzhen, China, October 13–17, 2019, Proceedings, Part IV 22*. Springer, 2019, pp. 629–638.
- [6] Z. Ning, Q. Xiao, Q. Feng, W. Chen, and Y. Zhang, "Relation-induced multi-modal shared representation learning for alzheimer's disease diagnosis," *IEEE Transactions on Medical Imaging*, vol. 40, no. 6, pp. 1632–1645, 2021.
- [7] D. Hu, H. Zhang, Z. Wu, F. Wang, L. Wang, J. K. Smith, W. Lin, G. Li, and D. Shen, "Disentangled-multimodal adversarial autoencoder: Application to infant age prediction with incomplete multimodal neuroimages," *IEEE transactions on medical imaging*, vol. 39, no. 12, pp. 4137–4149, 2020.
- [8] D. Hazarika, R. Zimmermann, and S. Poria, "Misa: Modality-invariant and-specific representations for multimodal sentiment analysis," in *Proceedings of the 28th ACM international conference on multimedia*, 2020, pp. 1122–1131.
- [9] J. Cheng, M. Gao, J. Liu, H. Yue, H. Kuang, J. Liu, and J. Wang, "Multimodal disentangled variational autoencoder with game theoretic interpretability for glioma grading," *IEEE Journal of Biomedical and Health Informatics*, vol. 26, no. 2, pp. 673–684, 2021.
- [10] Y. Li, Y. Wang, and Z. Cui, "Decoupled multimodal distilling for emotion recognition," in *Proceedings of the IEEE/CVF Conference on Computer Vision and Pattern Recognition*, 2023, pp. 6631–6640.
- [11] S. Zheng, Z. Zhu, Z. Liu, Z. Guo, Y. Liu, Y. Yang, and Y. Zhao, "Multimodal graph learning for disease prediction," *IEEE Transactions on Medical Imaging*, vol. 41, no. 9, pp. 2207–2216, 2022.
- [12] K. Hess, D. C. Spille, A. Adeli, P. B. Sporns, C. Brokinkel, O. Grauer, C. Mawrin, W. Stummer, W. Paulus, and B. Brokinkel, "Brain invasion and the risk of seizures in patients with meningioma," *Journal of Neurosurgery*, vol. 130, no. 3, pp. 789–796, 2018.
- [13] X. Li, Y. Lu, J. Xiong, D. Wang, D. She, X. Kuai, D. Geng, and B. Yin, "Presurgical differentiation between malignant haemangiopericytoma and angiomatous meningioma by a radiomics approach based on texture analysis," *Journal of Neuroradiology*, vol. 46, no. 5, pp. 281–287, 2019.
- [14] W. C. Chen, C.-H. G. Lucas, S. T. Magill, C. L. Rogers, and D. R. Raleigh, "Radiotherapy and radiosurgery for meningiomas," *Neuro-Oncology Advances*, vol. 5, no. Supplement_1, pp. i67–i83, 2023.
- [15] Z. Han, C. Zhang, H. Fu, and J. T. Z. Zhou, "Trusted multi-view classification," *arXiv preprint arXiv:2102.02051*, 2021.
- [16] Z. Han, C. Zhang, H. Fu, and J. T. Zhou, "Trusted multi-view classification with dynamic evidential fusion," *IEEE transactions on pattern analysis and machine intelligence*, vol. 45, no. 2, pp. 2551–2566, 2022.
- [17] Y. Zhang, J. Yang, J. Tian, Z. Shi, C. Zhong, Y. Zhang, and Z. He, "Modality-aware mutual learning for multi-modal medical image segmentation," in *Medical Image Computing and Computer Assisted Intervention–MICCAI 2021: 24th International Conference, Strasbourg, France, September 27–October 1, 2021, Proceedings, Part I 24*. Springer, 2021, pp. 589–599.
- [18] Z. Xing, L. Yu, L. Wan, T. Han, and L. Zhu, "Nestedformer: Nested modality-aware transformer for brain tumor segmentation," in *Medical Image Computing and Computer Assisted Intervention–MICCAI 2022: 25th International Conference, Singapore, September 18–22, 2022, Proceedings, Part V*. Springer, 2022, pp. 140–150.
- [19] J. Gao, T. Lyu, F. Xiong, J. Wang, W. Ke, and Z. Li, "Mggn: A multimodal graph neural network for predicting the survival of cancer patients," in *Proceedings of the 43rd International ACM SIGIR Conference on Research and Development in Information Retrieval*, 2020, pp. 1697–1700.
- [20] J.-H. Choi and J.-S. Lee, "Embracenet: A robust deep learning architecture for multimodal classification," *Information Fusion*, vol. 51, pp. 259–270, 2019.
- [21] R. Zhou, H. Zhou, B. Y. Chen, L. Shen, Y. Zhang, and L. He, "Attentive deep canonical correlation analysis for diagnosing alzheimer's disease using multimodal imaging genetics," in *International Conference on Medical Image Computing and Computer-Assisted Intervention*. Springer, 2023, pp. 681–691.
- [22] S. Li, Y. Xie, G. Wang, L. Zhang, and W. Zhou, "Adaptive multimodal fusion with attention guided deep supervision net for grading hepatocellular carcinoma," *IEEE Journal of Biomedical and Health Informatics*, vol. 26, no. 8, pp. 4123–4131, 2022.
- [23] Q. Zhu, H. Wang, B. Xu, Z. Zhang, W. Shao, and D. Zhang, "Multimodal triplet attention network for brain disease diagnosis," *IEEE Transactions on Medical Imaging*, vol. 41, no. 12, pp. 3884–3894, 2022.
- [24] P. Zhou, H. Chen, Y. Li, and Y. Peng, "Coco-attention for tumor segmentation in weakly paired multimodal mri images," *IEEE Journal of Biomedical and Health Informatics*, 2023.
- [25] R. A. Jacobs, M. I. Jordan, S. J. Nowlan, and G. E. Hinton, "Adaptive mixtures of local experts," *Neural computation*, vol. 3, no. 1, pp. 79–87, 1991.
- [26] A. Goyal, N. Kumar, T. Guha, and S. S. Narayanan, "A multimodal mixture-of-experts model for dynamic emotion prediction in movies," in *2016 IEEE International Conference on Acoustics, Speech and Signal Processing (ICASSP)*. IEEE, 2016, pp. 2822–2826.
- [27] B. Cao, Y. Sun, P. Zhu, and Q. Hu, "Multi-modal gated mixture of local-to-global experts for dynamic image fusion," in *Proceedings of the IEEE/CVF International Conference on Computer Vision*, 2023, pp. 23 555–23 564.
- [28] K. He, X. Zhang, S. Ren, and J. Sun, "Deep residual learning for image recognition," in *Proceedings of the IEEE conference on computer vision and pattern recognition*, 2016, pp. 770–778.
- [29] N. Bien, P. Rajpurkar, R. L. Ball, J. Irvin, A. Park, E. Jones, M. Bereket, B. N. Patel, K. W. Yeom, K. Shpanskaya *et al.*, "Deep-learning-assisted diagnosis for knee magnetic resonance imaging: development and retrospective validation of mrnet," *PLoS medicine*, vol. 15, no. 11, p. e1002699, 2018.
- [30] A. Adeli, K. Hess, C. Mawrin, E. M. S. Streckert, W. Stummer, W. Paulus, A. Kemmling, M. Holling, W. Heindel, R. Schmidt *et al.*, "Prediction of brain invasion in patients with meningiomas using preoperative magnetic resonance imaging," *Oncotarget*, vol. 9, no. 89, p. 35974, 2018.
- [31] L. Joo, J. E. Park, S. Y. Park, S. J. Nam, Y.-H. Kim, J. H. Kim, and H. S. Kim, "Extensive peritumoral edema and brain-to-tumor interface mri features enable prediction of brain invasion in meningioma: Development and validation," *Neuro-oncology*, vol. 23, no. 2, pp. 324–333, 2021.
- [32] U. Baid, S. Ghodasara, S. Mohan, M. Bilello, E. Calabrese, E. Colak, K. Farahani, J. Kalpathy-Cramer, F. C. Kitamura, S. Pati *et al.*, "The rsna-asnr-miccai brats 2021 benchmark on brain tumor segmentation and radiogenomic classification," *arXiv preprint arXiv:2107.02314*, 2021.
- [33] C. Davatzikos, S. Rathore, S. Bakas, S. Pati, M. Bergman, R. Kalarot, P. Sridharan, A. Gastouniotti, N. Jahani, E. Cohen *et al.*, "Cancer imaging phenomics toolkit: quantitative imaging analytics for precision diagnostics and predictive modeling of clinical outcome," *Journal of medical imaging*, vol. 5, no. 1, pp. 011 018–011 018, 2018.
- [34] A. Hatamizadeh, V. Nath, Y. Tang, D. Yang, H. R. Roth, and D. Xu, "Swin unetr: Swin transformers for semantic segmentation of brain tumors in mri images," in *International MICCAI Brainlesion Workshop*. Springer, 2021, pp. 272–284.

- [35] N. Srivastava, G. Hinton, A. Krizhevsky, I. Sutskever, and R. Salakhutdinov, "Dropout: a simple way to prevent neural networks from overfitting," *The journal of machine learning research*, vol. 15, no. 1, pp. 1929–1958, 2014.
- [36] Z. Zhong, L. Zheng, G. Kang, S. Li, and Y. Yang, "Random erasing data augmentation," in *Proceedings of the AAAI conference on artificial intelligence*, vol. 34, no. 07, 2020, pp. 13 001–13 008.
- [37] D. P. Kingma and J. Ba, "Adam: A method for stochastic optimization," *arXiv preprint arXiv:1412.6980*, 2014.
- [38] K. H. Brodersen, C. S. Ong, K. E. Stephan, and J. M. Buhmann, "The balanced accuracy and its posterior distribution," in *2010 20th international conference on pattern recognition*. IEEE, 2010, pp. 3121–3124.
- [39] F. Wilcoxon, "Individual comparisons by ranking methods," in *Breakthroughs in Statistics: Methodology and Distribution*. Springer, 1992, pp. 196–202.
- [40] Z. Xue and R. Marculescu, "Dynamic multimodal fusion," in *Proceedings of the IEEE/CVF Conference on Computer Vision and Pattern Recognition*, 2023, pp. 2574–2583.
- [41] L. Van der Maaten and G. Hinton, "Visualizing data using t-sne." *Journal of machine learning research*, vol. 9, no. 11, 2008.